Biomedical Optics EXPRESS

OCT angiography by absolute intensity difference applied to normal and diseased human retinas

Daniel Ruminski,[1,5] Bartosz L. Sikorski,[1,2,5] Danuta Bukowska,[1] Maciej Szkulmowski,[1] Krzysztof Krawiec,[3] Grazyna Malukiewicz,[2] Lech Bieganowski,[4] and Maciej Wojtkowski[1,*]

[1]*Institute of Physics, Faculty of Physics, Astronomy and Informatics, Nicolaus Copernicus University in Torun, Grudziadzka 5, 87-100 Torun, Poland*

[2]*Department of Ophthalmology, Nicolaus Copernicus University, 9 M. Sklodowskiej-Curie St., 85-094 Bydgoszcz, Poland*

[3]*Laboratory of Intelligent Decision Support Systems, Poznan University of Technology, Piotrowo 2, 60-965 Poznań, Poland*

[4]*Collegium Medicum, Nicolaus Copernicus University in Torun, Jagiellońska 13-15, 85-067 Bydgoszcz, Poland*

[5]*both authors contributed equally*

[*]*max@fizyka.umk.pl*

Abstract: We compare four optical coherence tomography techniques for noninvasive visualization of microcapillary network in the human retina and murine cortex. We perform phantom studies to investigate contrast-to-noise ratio for angiographic images obtained with each of the algorithm. We show that the computationally simplest absolute intensity difference angiographic OCT algorithm that bases only on two cross-sectional intensity images may be successfully used in clinical study of healthy eyes and eyes with diabetic maculopathy and branch retinal vein occlusion.

OCIS codes: (110.4500) Optical coherence tomography; (170.4470) Ophthalmology; (170.3880) Medical and biological imaging; (280.2490) Flow diagnostics.

References and links

1. R. K. Wang, S. L. Jacques, Z. Ma, S. Hurst, S. R. Hanson, and A. Gruber, "Three dimensional optical angiography," Opt. Express **15**(7), 4083–4097 (2007).
2. R. K. Wang and L. An, "Doppler optical micro-angiography for volumetric imaging of vascular perfusion in vivo," Opt. Express **17**(11), 8926–8940 (2009).
3. B. J. Vakoc, R. M. Lanning, J. A. Tyrrell, T. P. Padera, L. A. Bartlett, T. Stylianopoulos, L. L. Munn, G. J. Tearney, D. Fukumura, R. K. Jain, and B. E. Bouma, "Three-dimensional microscopy of the tumor microenvironment in vivo using optical frequency domain imaging," Nat. Med. **15**(10), 1219–1223 (2009).
4. A. Mariampillai, M. K. Leung, M. Jarvi, B. A. Standish, K. Lee, B. C. Wilson, A. Vitkin, and V. X. Yang, "Optimized speckle variance OCT imaging of microvasculature," Opt. Lett. **35**(8), 1257–1259 (2010).
5. V. J. Srinivasan, J. Y. Jiang, M. A. Yaseen, H. Radhakrishnan, W. Wu, S. Barry, A. E. Cable, and D. A. Boas, "Rapid volumetric angiography of cortical microvasculature with optical coherence tomography," Opt. Lett. **35**(1), 43–45 (2010).
6. V. J. Srinivasan, S. Sakadzić, I. Gorczynska, S. Ruvinskaya, W. Wu, J. G. Fujimoto, and D. A. Boas, "Quantitative cerebral blood flow with optical coherence tomography," Opt. Express **18**(3), 2477–2494 (2010).
7. J. Fingler, C. Readhead, D. M. Schwartz, and S. E. Fraser, "Phase-Contrast OCT Imaging of Transverse Flows in the Mouse Retina and Choroid," Invest. Ophthalmol. Vis. Sci. **49**(11), 5055–5059 (2008).
8. L. An, J. Qin, and R. K. Wang, "Ultrahigh sensitive optical microangiography for in vivo imaging of microcirculations within human skin tissue beds," Opt. Express **18**(8), 8220–8228 (2010).
9. A. Mariampillai, B. A. Standish, E. H. Moriyama, M. Khurana, N. R. Munce, M. K. Leung, J. Jiang, A. Cable, B. C. Wilson, I. A. Vitkin, and V. X. Yang, "Speckle variance detection of microvasculature using swept-source optical coherence tomography," Opt. Lett. **33**(13), 1530–1532 (2008).
10. W. J. Choi, R. Reif, S. Yousefi, and R. K. Wang, "Improved microcirculation imaging of human skin in vivo using optical microangiography with a correlation mapping mask," J. Biomed. Opt. **19**(3), 036010 (2014).
11. R. Leitgeb, L. Schmetterer, W. Drexler, A. Fercher, R. Zawadzki, and T. Bajraszewski, "Real-time assessment of retinal blood flow with ultrafast acquisition by color Doppler Fourier domain optical coherence tomography," Opt. Express **11**(23), 3116–3121 (2003).

#238344 Received 20 Apr 2015; revised 30 Jun 2015; accepted 30 Jun 2015; published 6 Jul 2015

12. S. Makita, Y. Hong, M. Yamanari, T. Yatagai, and Y. Yasuno, "Optical coherence angiography," Opt. Express **14**(17), 7821–7840 (2006).
13. L. An and R. K. Wang, "In vivo volumetric imaging of vascular perfusion within human retina and choroids with optical micro-angiography," Opt. Express **16**(15), 11438–11452 (2008).
14. A. Szkulmowska, M. Szkulmowski, D. Szlag, A. Kowalczyk, and M. Wojtkowski, "Three-dimensional quantitative imaging of retinal and choroidal blood flow velocity using joint Spectral and Time domain Optical Coherence Tomography," Opt. Express **17**(13), 10584–10598 (2009).
15. S. Makita, Y. Hong, M. Yamanari, T. Yatagai, and Y. Yasuno, "Optical coherence angiography," Opt. Express **14**(17), 7821–7840 (2006).
16. B. White, M. Pierce, N. Nassif, B. Cense, B. Park, G. Tearney, B. Bouma, T. Chen, and J. de Boer, "In vivo dynamic human retinal blood flow imaging using ultra-high-speed spectral domain optical coherence tomography," Opt. Express **11**(25), 3490–3497 (2003).
17. M. Szkulmowski, I. Grulkowski, D. Szlag, A. Szkulmowska, A. Kowalczyk, and M. Wojtkowski, "Flow velocity estimation by complex ambiguity free joint Spectral and Time domain Optical Coherence Tomography," Opt. Express **17**(16), 14281–14297 (2009).
18. M. Szkulmowski, A. Szkulmowska, T. Bajraszewski, A. Kowalczyk, and M. Wojtkowski, "Flow velocity estimation using joint Spectral and Time domain Optical Coherence Tomography," Opt. Express **16**(9), 6008–6025 (2008).
19. B. Braaf, K. A. Vermeer, K. V. Vienola, and J. F. de Boer, "Angiography of the retina and the choroid with phase-resolved OCT using interval-optimized backstitched B-scans," Opt. Express **20**(18), 20516–20534 (2012).
20. S. Zotter, M. Pircher, T. Torzicky, M. Bonesi, E. Götzinger, R. A. Leitgeb, and C. K. Hitzenberger, "Visualization of microvasculature by dual-beam phase-resolved Doppler optical coherence tomography," Opt. Express **19**(2), 1217–1227 (2011).
21. S. Makita, F. Jaillon, M. Yamanari, M. Miura, and Y. Yasuno, "Comprehensive in vivo micro-vascular imaging of the human eye by dual-beam-scan Doppler optical coherence angiography," Opt. Express **19**(2), 1271–1283 (2011).
22. I. Grulkowski, I. Gorczynska, M. Szkulmowski, D. Szlag, A. Szkulmowska, R. A. Leitgeb, A. Kowalczyk, and M. Wojtkowski, "Scanning protocols dedicated to smart velocity ranging in spectral OCT," Opt. Express **17**(26), 23736–23754 (2009).
23. K. Kurokawa, K. Sasaki, S. Makita, Y.-J. Hong, and Y. Yasuno, "Three-dimensional retinal and choroidal capillary imaging by power Doppler optical coherence angiography with adaptive optics," Opt. Express **20**(20), 22796–22812 (2012).
24. R. K. Wang, L. An, P. Francis, and D. J. Wilson, "Depth-resolved imaging of capillary networks in retina and choroid using ultrahigh sensitive optical microangiography," Opt. Lett. **35**(9), 1467–1469 (2010).
25. T. Schmoll, A. S. G. Singh, C. Blatter, S. Schriefl, C. Ahlers, U. Schmidt-Erfurth, and R. A. Leitgeb, "Imaging of the parafoveal capillary network and its integrity analysis using fractal dimension," Biomed. Opt. Express **2**(5), 1159–1168 (2011).
26. J. Fingler, R. J. Zawadzki, J. S. Werner, D. Schwartz, and S. E. Fraser, "Volumetric microvascular imaging of human retina using optical coherence tomography with a novel motion contrast technique," Opt. Express **17**(24), 22190–22200 (2009).
27. J. Fingler, D. Schwartz, C. Yang, and S. E. Fraser, "Mobility and transverse flow visualization using phase variance contrast with spectral domain optical coherence tomography," Opt. Express **15**(20), 12636–12653 (2007).
28. R. Motaghiannezam and S. Fraser, "Logarithmic intensity and speckle-based motion contrast methods for human retinal vasculature visualization using swept source optical coherence tomography," Biomed. Opt. Express **3**(3), 503–521 (2012).
29. Y. Jia, O. Tan, J. Tokayer, B. Potsaid, Y. Wang, J. J. Liu, M. F. Kraus, H. Subhash, J. G. Fujimoto, J. Hornegger, and D. Huang, "Split-spectrum amplitude-decorrelation angiography with optical coherence tomography," Opt. Express **20**(4), 4710–4725 (2012).
30. D. Ruminski, D. Bukowska, I. Gorczynska, M. Szkulmowski, and M. Wojtkowski, "Angiogram visualization and total velocity blood flow assessment based on intensity information analysis of OCT data," Proc. SPIE **8213**, 821306 (2012).
31. H. C. Hendargo, R. Estrada, S. J. Chiu, C. Tomasi, S. Farsiu, and J. A. Izatt, "Automated non-rigid registration and mosaicing for robust imaging of distinct retinal capillary beds using speckle variance optical coherence tomography," Biomed. Opt. Express **4**(6), 803–821 (2013).
32. J. Xu, K. Wong, Y. Jian, and M. V. Sarunic, "Real-time acquisition and display of flow contrast using speckle variance optical coherence tomography in a graphics processing unit," J. Biomed. Opt. **19**(2), 026001 (2014).
33. D. M. Schwartz, J. Fingler, D. Y. Kim, R. J. Zawadzki, L. S. Morse, S. S. Park, S. E. Fraser, and J. S. Werner, "Phase-variance optical coherence tomography: a technique for noninvasive angiography," Ophthalmology **121**(1), 180–187 (2014).
34. Y. Jia, S. T. Bailey, D. J. Wilson, O. Tan, M. L. Klein, C. J. Flaxel, B. Potsaid, J. J. Liu, C. D. Lu, M. F. Kraus, J. G. Fujimoto, and D. Huang, "Quantitative Optical Coherence Tomography Angiography of Choroidal Neovascularization in Age-Related Macular Degeneration," Ophthalmology **121**(7), 1435–1444 (2014).

#238344 Received 20 Apr 2015; revised 30 Jun 2015; accepted 30 Jun 2015; published 6 Jul 2015

35. Y. Jia, E. Wei, X. Wang, X. Zhang, J. C. Morrison, M. Parikh, L. H. Lombardi, D. M. Gattey, R. L. Armour, B. Edmunds, M. F. Kraus, J. G. Fujimoto, and D. Huang, "Optical Coherence Tomography Angiography of Optic Disc Perfusion in Glaucoma," Ophthalmology **121**(7), 1322–1332 (2014).
36. D. Y. Kim, J. Fingler, J. S. Werner, D. M. Schwartz, S. E. Fraser, and R. J. Zawadzki, "In vivo volumetric imaging of human retinal circulation with phase-variance optical coherence tomography," Biomed. Opt. Express **2**(6), 1504–1513 (2011).
37. C. Blatter, T. Klein, B. Grajciar, T. Schmoll, W. Wieser, R. Andre, R. Huber, and R. A. Leitgeb, "Ultrahigh-speed non-invasive widefield angiography," J. Biomed. Opt. **17**(7), 070505 (2012).
38. J. Lee, V. Srinivasan, H. Radhakrishnan, and D. A. Boas, "Motion correction for phase-resolved dynamic optical coherence tomography imaging of rodent cerebral cortex," Opt. Express **19**(22), 21258–21270 (2011).
39. M. Wojtkowski, B. L. Sikorski, I. Gorczynska, M. Gora, M. Szkulmowski, D. Bukowska, J. Kaluzny, J. G. Fujimoto, and A. Kowalczyk, "Comparison of reflectivity maps and outer retinal topography in retinal disease by 3-D Fourier domain optical coherence tomography," Opt. Express **17**(5), 4189–4207 (2009).
40. B. L. Sikorski, D. Bukowska, J. J. Kaluzny, M. Szkulmowski, A. Kowalczyk, and M. Wojtkowski, "Drusen with accompanying fluid underneath the sensory retina," Ophthalmology **118**(1), 82–92 (2011).
41. G. Bradski, "The OpenCV Library (2000)," Dr. Dobbs J. Softw. Tools Prof. Program. (2000).

1. Introduction

The visualization and assessment of retinal microcirculation is of immense significance for both scientific and clinical purposes because it may be indicative for such pathological conditions asischemia and inflammation. Therefore, it is potentially very useful for diagnosis and monitoring of individuals with diabetes, retinal artery and vein occlusion, arterial hypertension, and other vascular disorders.

For last several decades fluorescein angiography (FA) has been a basic clinical diagnostic imaging technique used for visualization of retinal microcapillaries. FA allows direct measurement of blood flow in retinal vasculature by recording the fluorescence signal coming from fluorescein delivered intravenously. That is why it easily reveals the areas of occlusion and non-perfusion. It also enables dynamic observation of dye extravasation thus helping to identify leaking vessels. However, apart from obvious benefits, FA has one major disadvantage. It is an invasive technique and requires fluorescein dye injection that can trigger allergic reactions. Therefore, the use of FA is not recommended in pregnant women, children and individuals with known allergies. Additionally, the procedure should not be repeated at short time intervals.

Unlike to FA, optical coherence tomography (OCT) is a non-invasive and non-contact technique widely used to image the fundus of the eye. Apart of 3D structural imaging it has been employed in quantitative and qualitative studies of hemodynamics in rodent brains [1–6] and retinas [7], skin [8–10] as well as human fundus [11–14]. Quantitative blood flow velocity measurement is available generally using Doppler OCT technique [11, 15–18]. Unfortunately, although theoretically possible, the quantitative information about microcapillary flow is not easy to obtain by this method. The reason of poor sensitivity of quantitative Doppler OCT applied to the retina is that in most cases the orientation of blood vessels is almost perpendicular to the direction of the scanning beam, as a result the slowest motions become obscured by noise. To push beyond conventional Doppler OCT imaging limitations several groups have developed alternative scanning protocols. For example the visibility of small vessels has been improved by increasing time span between analyzed measurements [19–23] and enhanced Doppler contrast has been used for qualitative visualization of *enface* maps [19, 20, 22, 23].

Recently, alternative method to visualize microvasculature (called OCT angiography) has been established. This technique does not depend on the orientation of blood vessels and is derived from the fluctuation of the backscattered light modulated by the flowing particles. The time scale of random fluctuations in the dynamic scattering component is related to blood cells velocity. Thus, it requires collection of more than one A-scan or the entire B-scan registered at the same spatial position of the scanning beam for calculating the flow motion contrast. The OCT angiography modalities enabling retinal microvasculature imaging include: optical microangiography (OMAG) [24], spatial tomogram filtration [25], variance

#238344 Received 20 Apr 2015; revised 30 Jun 2015; accepted 30 Jun 2015; published 6 Jul 2015

of phase shifts [26], (circular) phase variance [3, 27], dual-beam scanning [20, 21], amplitude and intensity analysis [5, 10, 28], absolute complex difference [5], intensity decorrelation [29] and speckle variance methods [9, 30–32]. However, each of them has varying capabilities in regard to microvascular visualization, noise levels, artifacts, field of view and imaging speed while imaging retina. In this context, further improvement of OCT angiography is still required to be applicable for daily clinical application at the level comparable with FA.

Recent reports show that phase-resolved method is capable to visualize retinal microvasculature using only two oversampled data sets [19–21]. However, human retinal diseases imaging is rather performed with modalities employing multiple data oversampling [25, 33–35]. Exemplary, phase variance technique applied to patients with retinal diseases uses from 5 to 10 consecutive B-scans in order to give one flow contrasted B-scan [26, 33, 36]. Since phase-based methods very often require very precise removal of background Doppler phase shifts due to the axial movement of bulk tissue other research groups have focused on improvement of amplitude-based OCT signal analysis. Jiaet al. presented an improved amplitude-based OCT angiography algorithm. The algorithm called "split-spectrum amplitude-decorrelation angiography" (SSADA) requires collection of 8 [29] or 4 B-scans from one spatial location [34, 35]. Splitting the spectrum reduces the predominant bulk-motion noise in the axial dimension where OCT resolution is higher than that in the transverse dimension. J. Xu et al. has shown that the speckle variance algorithm may advance imaging speed to reach real-time imaging in mouse and human eyes *in vivo* [32].

Dedicated algorithms for 2D flow maps integration into wide-field mosaic has been also already presented [31], but still need to be verified on medical cases. Another work shows, that high speed FDML technology is capable to provide 48 degree OCT angiography preview without the need of image stitching [37] and nearly free from motion artifacts. Unfortunately, system requires specific not yet commercially available light sources.

In this study we compare four out of OCT angiographic techniques mentioned before: phase variance [3, 27], absolute complex difference [5], speckle variance [9] and absolute intensity difference (AID) [5, 10] in terms of sensitivity for small capillary detection, resistance to bulk tissue motion and computational complexity in different practical situations, where total acquisition time is a key factor. The analysis was performed with different number of A-scans used to calculate one angio-OCT tomogram line: in case where acquisition time is not crucial (like in murine brain imaging) and where it is crucial, like in ophthalmic imaging. For the latter we compared the variations of the techniques with only two A-scans used for calculations. The latter analysis show very similar visualization performance for each of the method. Due to this fact we select computationally the simplest AID technique to show for the first time to our knowledge its applicability to clinical studies of healthy eyes and eyes with diabetic maculopathy and branch retinal vein occlusion. Results have been compared with FA. Further, an original fully automated algorithm is presented to facilitate the assembly of a mosaic of overlapping *en face* OCT angiograms.

2. Methods

2.1 Imaging of the human eye

The OCT retinal imaging instrument employed in this study was designed and developed at Nicolaus Copernicus University. The device used superluminescent diode as a light source (λ_C = 820nm, $\Delta\lambda$ = 70nm, Broadlighter D830 Superlum,) provided an axial resolution of4.5 μmin sample. In the sample arm, the beam diameter on the cornea equaled to 2.1 mm and a diameter of the spot focused on the retinal plane was estimated as ~13 μm. The OCT signal was detected by a custom-designed spectrometer containing a collimating lens, a volume holographic diffraction grating (1200 lines⁄mm; Wasatch Photonics), a telecentric f-theta lens (effective focal length 79.6 mm; Sill Optics), and a 12-bit CMOS line scan camera (spl4096-140 km, Basler Sprint). We used 1280 of 4096 pixels available in the camera and provided

#238344 Received 20 Apr 2015; revised 30 Jun 2015; accepted 30 Jun 2015; published 6 Jul 2015

high imaging speeds (100 000 axial scans/s for 8.6 μs exposure time per A-scan). With 750 μW power on the sample, measured sensitivity of the system was 91 dB.

The fixation target was displayed in the imaging path of the OCT system. A grid of fixation marks printed on a diffusive transparency plate was illuminated with a white light and optically filtered to pass only the red part of the halogen lamp emission spectrum. By focusing their gaze on subsequent fixation marks, patients exposed the required retinal area to the OCT imaging beam in a series of consecutive measurements. As a result, mosaics of 3-D OCT images were combined. The red background of the fixation target also helped to minimize the distractive effect of the OCT imaging beam visible as a moving red spot, thus reducing eye motion artifacts in OCT tomograms. The study protocol compliant with Declaration of Helsinki was approved by the Internal Review Board of the Nicolaus Copernicus University. We recruited fifteen healthy volunteers and seventeen individuals with DM and 5 with BRVO. All patients were enrolled based on clinical assessment. Chosen subjects were regular clinical patients without any additional selection of eye stability or cooperativity. Exclusion criteria included visual acuity <20/200, and media opacity interfering with OCT image quality, such as cataract. The eye examination included color fundus photographs, FA and OCT. FA was performed using Topcon TRC-50DX IA device (Topcon, Japan). For OCT imaging patients pupils were dilated with 1% Tropicamidium.

2.2 The murine brain imaging system

Retinal imaging is a challenging task because of involuntary movement of the eye during acquisition time. In order to test performance of the various OCT angiography techniques we decided to compare results of the retinal imaging (always affected by object motion) with nearly motion free imaging of the vasculature of the mouse brain *in vivo*. For this purpose an OCT microscopic system was developed and constructed by our group. The instrument operated at imaging speeds of 100 000 axial scans/s. Light emitted by the femtosecond laser (λc = 790 nm, $\Delta\lambda$ = 150 nm, Femto lasers, Australia) provided the measured axial resolution of 2 μm in tissue. After passing the isolator and entering the fiber coupler, the light was split between the reference and object arm. For the optimization of the instrument sensitivity 80% of light was directed to the reference arm and 20% to the object arm. The reference arm contained polarization control, dispersion compensation and light attenuation. In the object arm the light emerging from the optical fiber was collimated using 20x Olympus PlanN objective (L1 = 9mm) and directed to two lenses (L2 and L3, f2 = 54 mm, f3 = 75 mm). Objective lens (Thorlabs scan objective 10x (L4, f = 18mm) allowed for murine brain imaging with the lateral resolution ~7.85 μm and depth of focus 117 μm. With 750 μW power on the sample, measured sensitivity of the system is 95 dB.

Animal handling protocols were in compliance with the Ethical Committee of Animal Research of the Nencki Institute of Experimental Biology, Polish Academy of Sciences, based on European Union regulations. To obtain high quality images in deeper areas of the brain, one week before the OCT session, the scalp and underlying periosteum of adult female C57BL/6 mice were gently removed from skull bone. The selected skull area (the center) was carefully thinned and the glass window was built in the live mouse brain. During the OCT session the mouse was anesthetized and immobilized in a stereotactic device. The body temperature was kept at 37°C throughout the experiments. Animal studies were performed by investigation stereotactic stabilized murine cerebral structures. This step was due to test different protocols and data processing algorithms in a more controlled, precise and systematic conditions.

2.3. OCT angiographic algorithms

In order to find the fastest and computationally efficient OCT angiographic technique we identified four best candidates from existing methods: phase variance [3, 27], absolute complex difference [5], speckle variance [9] and absolute intensity difference (AID) [5, 10]

#238344 Received 20 Apr 2015; revised 30 Jun 2015; accepted 30 Jun 2015; published 6 Jul 2015

and applied them to the same set of OCT data. In each case the final flow contrasted B-scan was generated from N complex-valued OCT signals A(x, z, t) taken from consecutively acquired (oversampled) B-scans. Here, N is even, variables x and y denote lateral position on the sample while variable t stands for time.

In the phase variance algorithm (PV) [3, 27] for each pair of consecutive B-scans a complex product is calculated and weighted by inverse of mean signal magnitude. Next circular variance is calculated over K pixels along in-depth (z direction). At the end the result is averaged over all B-scan pairs:

$$I_{PV}(x,z) = M_{mean}^2(x,z)\frac{1}{N/2}\sum_{i=0}^{\frac{N}{2}-1}\left(1-\left|\sum_{z'=0}^{K-1}\frac{A(x,z-z',t_{2i+1})A^*(x,z-z',t_{2i})}{\left|A(x,z-z',t_{2i})\right|^2}\right|\right). \quad (1)$$

In this study we calculated variance over K = 10 pixels (45 μm) in depth [3, 27]. Averaging can be also successfully applied along lateral x direction, instead or additionally to averaging in z direction, but it would decrease lateral resolution. Phase noise highly depends on signal-to-noise ratio (SNR), therefore data should be first selected by a simple threshold operation: I_{PV} is multiplied by squared averaged signal amplitude M_{mean} (Eq. (2).

$$M_{mean}(x,z) = \frac{1}{N}\sum_{i=0}^{N-1}\left|A\left(x,z,t_i\right)\right|. \quad (2)$$

Second algorithm is named absolute complex difference (ACD) and is calculated as an amplitude of complex difference between each pair of B-scans, averaged over all pairs:

$$I_{ACD}(x,z) = \left(\frac{1}{N/2}\sum_{i=0}^{\frac{N}{2}-1}\left|A\left(x,z,t_{2i+1}\right)-A\left(x,z,t_{2i}\right)\right|\right)^2. \quad (3)$$

This method is highly sensitive to bulk motion of the eye. In order to keep high contrast of capillary image ACD requires at least axial phase shift motion compensation [38].

The third algorithm is speckle variance (SV) [9], calculated as variance of OCT signal intensity (here M(x,z,t) = |A(x,z,t)|):

$$I_{SV}(x,z) = \frac{1}{N}\sum_{i=0}^{N-1}\left(M\left(x,z,t_i\right)-M_{mean}\left(x,z\right)\right)^2. \quad (4)$$

The last approach is to calculate mean absolute intensity difference (AID) between each pair of consecutive B-scans [5]:

$$I_{AID}(x,z) = \left(\frac{1}{N/2}\sum_{i=0}^{\frac{N}{2}-1}\left|M\left(x,z,t_{2i+1}\right)-M\left(x,z,t_{2i}\right)\right|\right)^2. \quad (5)$$

All of the above mentioned methods were applied to the same set of data. As a result, from N times oversampled B-scan we finally obtained one structural (squared M_{mean}) and 4 flow (I_{PV}, I_{ACD}, I_{SV}, I_{AID}) B-scans (Fig. 1(b)). All tomograms were mapped onto logarithmic scale and were converted to 8-bit gray scale images after histograms equalization. Above procedures were iteratively applied to the entire three-dimensional data set.

In order to compare the algorithms in time critical situations, like ophthalmic imaging, we designed scanning protocols that collect only two B-scans at the same spatial location (N = 2) with the same sampling density over the fast (x) and slow (y) scanning axes. The scanning was performed in a saw-tooth raster pattern, but each position along the slow (y) axis was oversampled two times. In order to retrieve sufficient information about the retinal microcapillary network from different retinal layers, 720 cross-sectional B-scans, each consisted of 360 A-scans, were collected. A 3D scan (x-y-z) covered a volume of 3.1 mm x

#238344 Received 20 Apr 2015; revised 30 Jun 2015; accepted 30 Jun 2015; published 6 Jul 2015

3.1 mm x 2.1 mm (**protocol A**). To visualize vessels from larger area on the retina we collected 480 cross-sectional images, each B-scan consisted of 240 A-scans. A 3D scan covered an area of 1.5 mm x 1.5 mm x 2.1 mm (**protocol B**). The procedure was repeated usually 9 times for neighboring areas and the results were stitched to create a mosaic of total size of 4.5 x 4.5 mm on the retina. The last protocol (**protocol C**), required for high-resolution structural imaging, collected20 cross-sectional images, each consisting of 20,000 A-scans acquired in less than 5 seconds and covering an area 7 mm x 7 mm x 2.1 mm.

To compare the algorithms for conditions when total acquisition time allows for higher oversampling we modified protocol B. In case of the retinal imaging one volumetric scan of healthy volunteer was performed and analyzed, with the scanning parameters: x = 1.5 mm, y = 1.5 mm and z = 2.1 mm, and N = 8 (**protocol D**). For the animal study we chose x = 2 mm, y = 2 mm, z = 1.5 mm and N = 6 (**protocol E**). All protocols are summarized in Table 1.

Table 1. Scanning protocols list.

Parameters	Protocol				
	A	B	C	D	E
Scanning area: x,y,z [mm^3]	3.1 × 3.1 × 2.1	1.5 × 1.5 × 2.1	7 × 7 × 2.1	1.5 × 1.5 × 2.1	2 × 2 × 1.5
Number of acquired B-scans	720	480	20	1920	1440
Number of M-B frames	2	2	1	8	6
Number of generated flow B-scans	360	240	-	240	240
Number of A-scans/B-scan	360	240	20,000	240	240
Total acquisition time [s]	2.8	1.3	4	5.2	4

2.4. Quantification of OCT angiographic procedures

In order to propose a quantitative and objective parameters describing applicability of the vasculature detection algorithms, we performed fully controlled experiment using a silicon capillary (280 μm I.D.) filled with 2% intralipid solution. The phantom was placed on a silicone rubber (Elastosil RT 601) with added TiO_2powder. The capillary was immersed with silicone and covered with coverslip. Intralipid solution was pumped through capillary with a syringe pump at constant flow rate of 2 ml/h. Measurements were performed on the ophthalmic setup combined with additional f = 30 mm lens in the objective arm. Consecutive unidirectional tomograms were gathered firstly from the same spatial location, secondly with 0.2 μm shift (lateral resolution 15 μm) in lateral direction in order to simulate object motion and increase decorrelation between oversampled B-scans. Each B-scan consists of 2200 A-scans and covers x = 400μm. Quantitative comparison of different vasculature detection algorithms was applied by contrast to noise ratio calculation CNR (Eq. (6). Signal (I_S) and noise (I_N) are as were selected manually. CNR for different algorithms was tested according to increasing number of oversampled B-scans. A similar way of analyzing data has been already performed by other group to test speckle variance algorithm performance [4].

$$CNR_{S/N} = \frac{\overline{I_S} - \overline{I_N}}{\sqrt{\sigma_S^2 + \sigma_N^2}}. \tag{6}$$

To give a reasonable comparison of OCT angiography algorithms we choose visualization quality indicators as: resistance to hyper-reflective static structures, sensitivity for small capillaries, resistance to subject motion, total acquisition time, and algorithm computational complexity and assessed flow visualization improvement by calculating the contrast to noise ratio. We also assessed algorithms complexity in terms of computational time.

#238344 Received 20 Apr 2015; revised 30 Jun 2015; accepted 30 Jun 2015; published 6 Jul 2015

2.5. Flow map visualization

We applied a custom-designed automatic retinal layer segmentation algorithm to create *en face* flow maps (angiograms). First, the position of the retinal pigment epithelium (RPE) was detected [39, 40]. Then, data cropping was performed to remove unwanted scattering IS/OS and RPE layers, see Fig. 1(c). This step was necessary due to imperfections of the OCT angiography algorithms (highly scattering signals were not fully suppressed by these methods in the case of eye movement).In order to present *enface* projection of capillary bed seen in Fig. 1(d) maximum intensity projection MIP was taken from volumetric flow B-scans set, see Fig. 1(a). The rendering was performed using commercially available software Amira 4.1 (Vissage Imaging GmbH, Berlin, Germany). Additionally, to enhance visualization, the 3D angiogram was separately projected into *en face* views in 3 layers using manual segmentation. The large retinal vessels layer corresponds to the nerve fiber layer. The superficial capillary plexus corresponds to the ganglion cell layer. The deep capillary plexus layer was defined as inner nuclear layer. All of boundaries were identified through the analysis of the reflectance and reflectance-gradient profiles in depth. Separate *en face* images were coded in false-colors and then put together to create a depth color-coded projection.

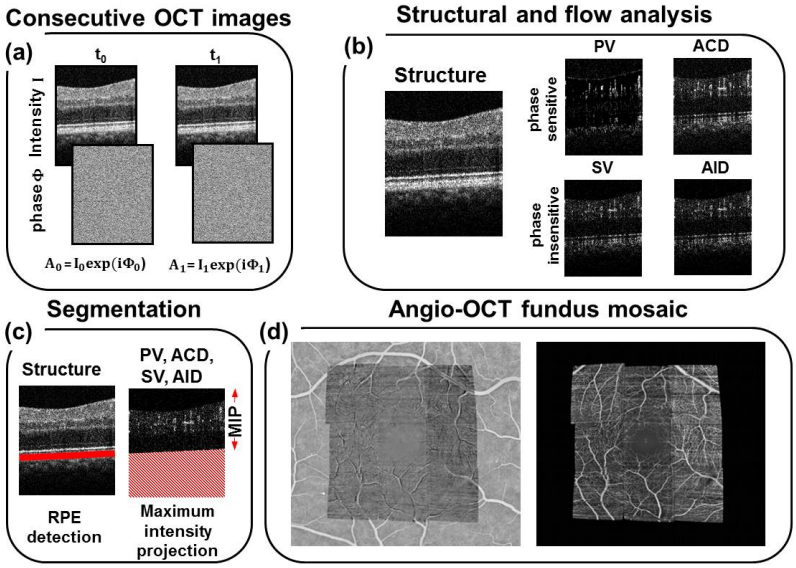

Fig. 1. The 2D OCT image processing procedure for visualizing retinal microcapillary network (protocol B). (a)Set of 2 oversampled OCT cross-sectional images measured at the same retinal location. (b) Structural and angiographic cross-sectional images (PV - phase variance, ACD - absolute complex difference, SV- speckle variance, AID - absolute intensity difference. (c) A scheme of custom-designed automatic retinal layer segmentation algorithm. (d) *Enface* view of the retinal vasculature acquired using the maximum intensity projections MIP of all differential images from nine 3D OCT data sets. Picture on the left: Angio-OCT mosaic projected onto the FA image.

2.6. Wide-field mosaic assembly algorithm

We collected a set of multiple, three-dimensional data to cover a larger area of the retina with vascular maps. After data processing as described in paragraph *2.5.*, the individual angiographic maps were automatically merged into one large mosaic angio-OCT fundus image. The objective of the assembly algorithm was to spatially co-register a set of *en face* OCT visualizations and the corresponding FA image to each other so that the blood vessels were aligned. This task is non-trivial, given the substantial differences in image acquisition

#238344 Received 20 Apr 2015; revised 30 Jun 2015; accepted 30 Jun 2015; published 6 Jul 2015

between the two techniques. Below, we present the conceptual overview of the proposed algorithm, as its complete technical description is beyond the scope of this paper.

The algorithm starts with initial preprocessing. Because FA images are usually darker in perifoveal area due to lower density of imaged blood vessels, we leveled out the spatial brightness variance by subtracting a background image obtained by Gaussian filtering. The OCT images were scaled to match the spatial resolution of FA image. The bright horizontal stripes resulting from eye movements between B-scans were dimmed (if present) by a factor estimated from the neighboring rows of pixels.

After preprocessing, the algorithm was elastically co-registering ('warping') each of the OCT images independently against the corresponding region in the FA image. Co-registration consisted of superposition of translation, rotation, scaling, and collinear distortion; these transformations were expressed by a 3x3 (augmented) *affine transformation matrix*. The algorithm started with an initial content of the matrix, determined by an approximate manual matching that involved only translation, and was refining it iteratively. In each iteration, the algorithm attempted to improve the current transformation by independently increasing and decreasing the particular elements of the matrix (transformation coefficients). As affine transformation varies in its sensitivity to particular coefficients, *step sizes* have been individually pre-tuned for particular coefficients in a preliminary experiment. As a result, the step sizes for, e.g., the coefficients responsible for collinear distortion were several orders of magnitude smaller than those for translation.

On a higher abstraction level, this iterative improvement can be phrased as an optimization process, where each matrix is a *candidate solution* in a *search space* of all 3x3 affine transformation matrices. The task of the search algorithm was to optimize the assumed quality measure, i.e., maximize the pixelwise cross correlation of the transformed OCT image with A. In each iteration, from the current matrix M, a set of *neighbors* (matrices) M_i is created by adding and subtracting the abovementioned step sizes to particular coefficients in M. Given 8 modifiable elements (the lower-right element of the augmented affine transformation matrix is always 1) and two possible directions (increment and decrement), there were 16 neighbors M_i, $i = 1,\ldots,16$, generated in each such step. For each M_i, the OCT image was transformed according to M_i and its cross correlation with the AF image was calculated. The neighbor with the highest cross-correlation replaced the current matrix M, and was the starting point for the next iteration. Such *local search* is one of possible heuristic approaches in situations where the dependency of the optimized function (cross-correlation) on the independent variables (matrix coefficients) is unknown or difficult to model analytically, which is the case here.

The search iterated until no move improved cross-correlation anymore, i.e., cross-correlation was for all M_is worse (larger) than for current M. Then, the steps sizes were halved to make the adjustments more fine-grained. The optimization continued until no further improvement could be made, at which point step sizes were halved again. When, in consequence of consecutive reductions, step sizes achieved predefined lower limits, the algorithm was terminating and the final best-found transformation matrix was used to finally warp the OCT image, which was then overlaid with the AF image, as shown in Fig. 1(d) (in two variants).

The several OCT images co-registered with the FA image by means of the above optimization algorithm formed the final mosaic. The pixels where two or more warped OCT images overlap were subject to additional post processing which reconciled the possible inconsistencies between the OCT images, so that the boundaries between them were often barely visible as seen in Fig. 1(d).

All calculations were carried out with subpixel precision to minimize sampling error incurred by finite image resolution (raster). Warping used bicubic interpolation to minimize the error resulting from aliasing. The assembly algorithm was implemented in C++ with the computer vision library OpenCV [41]. Apart from the initial positioning of OCT images, it

#238344 Received 20 Apr 2015; revised 30 Jun 2015; accepted 30 Jun 2015; published 6 Jul 2015

operated autonomously and does not require human intervention. Usually, it required a dozen up to a hundred of iterations, which took seconds on contemporary PCs.

3. Results

3.1 The quantitative comparison of OCT angiography algorithms

To compare performance of the algorithms in a fully controlled experiment, enabling a precise detection of moving components, we used a capillary phantom described in paragraph *2.4*. Referring to paragraph *2.3*, we have chosen three regions of interest seen in Fig. 2(a) and we looked at the resistance to subject motion or to hyper reflective layers and the sensitivity to small capillaries. CNR contrast was calculated between flow area (I_S) and two regions corresponding to different definitions of noise: hyper-reflective static structure (I_{N1}), background noise (I_{N2}). We compared original algorithms described in paragraph *2.3* versus number of N oversampled B-scans and plotted results as solid lines on panels b-d in Fig. 2.

As it was mentioned in paragraph *2.3* in the PV algorithm the circular variance is calculated over K pixels along in-depth (z direction). Therefore, in contrast to other three techniques PV gives automatically projection in z-direction. Usually OCT angiography data is also displayed as *enface* projection views by averaging a few *enface* C-scans. In order to include the projection display mode in our quantitative validation we uniformed the resolution between all methods. Each flow B-scan (I_{SV},I_{AID},I_{ACD}) was averaged with rectangular window spatially equal to those used for PV circular variance calculation. For this averaging procedure we did not provide any additional phase stabilization procedures. Results after additional averaging are shown as dashed lines in Fig. 2.

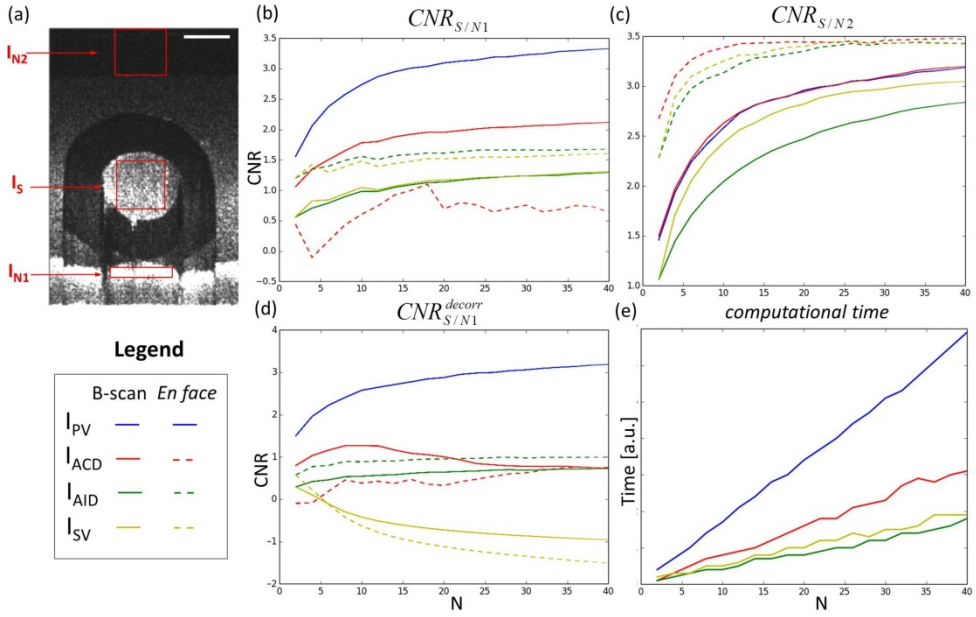

Fig. 2. Comparison of contrast to noise ratio CNR for different OCT angiography algorithms. (a) Exemplary intensity B-scan image. Red rectangles indicate regions of interest to CNR calculation: flow area (I_S), hyper-reflective static structure (I_{N1}) and noise background (I_{N2}). Scale bar: 100 µm. (b) CNR calculated from I_S and I_{N1} versus number of oversampled B-scans. (c) CNR calculated from I_S and I_{N2}. (d) CNR calculated between I_S and I_{N1} in the case of object motion (additionally decorrelated B-scans). (e) Computational time of given algorithm versus number of oversampled B-scans. Dashed lines correspond *to enface* projection display mode - CNR calculated based on averaging in z direction. I_{PV} - phase variance (blue solid line), I_{ACD} - absolute complex difference with and without axial phase compensation (red solid/dashed line), I_{SV} -speckle variance (yellow solid/dashed line), absolute intensity difference I_{AID} (green solid/dashed line).

#238344 Received 20 Apr 2015; revised 30 Jun 2015; accepted 30 Jun 2015; published 6 Jul 2015

The first parameter – the resistance to hyper-reflective static structures is compared in Figs. 2(b) and 2(d). The best performance in this case has phase variance algorithm (blue solid line). Differences between AID and SV algorithms are very subtle as seen in Fig. 2(b). However, the experiment was performed in perfectly stable conditions without any motion of the object. In order to take into account additional influence of bulk motions we introduced a decorrelation of the consecutive oversampled B-scans (Fig. 2(d)). Also in this case the phase variance algorithm has the best performance but now the difference between AID and SV is more profound – SV algorithm is much more sensitive to the object motion, especially for the larger number of oversampled B-scans (solid green and yellow lines in Fig. 2(d)). For the projection mode (dashed lines) the performance of AID and SV methods is improved for both techniques only in the static case. In the case of the object motion AID technique shows its advantage even over the ACD. Lack of phase stabilization in ACD degrades contrast seriously as seen in Fig. 2(b), 2(d).

In order to examine the sensitivity to detect motion we computed CNR between I_S and I_{N2} areas. In this comparison PV and ACD present very similar result seen in Fig. 2(c) (solid blue and red lines). Additional averaging for SV, AID and ACD analysis improves their contrast significantly ($CNR_{S/N2}$) between flow and background noise areas in all of these methods (Fig. 2(c) dashed lines). The largest benefit of *en face* projection is visible for AID technique, that has almost a similar performance to SV and AID. It has to be stressed that AID and SV for N = 2give the same contrast values as seen in Fig. 2(b)-2(d).

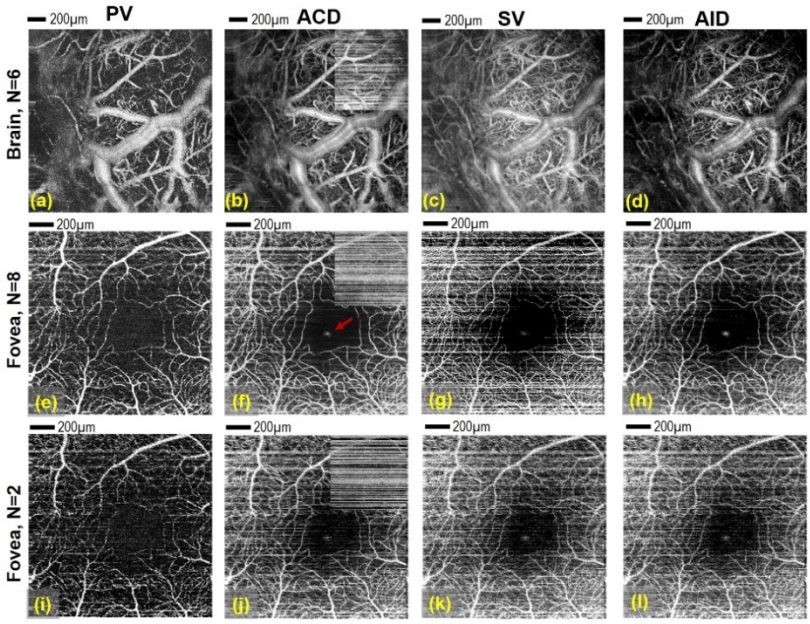

Fig. 3. Presentation of angio-OCT maps obtained from two data sets (I – mouse brain (a-d) measured with protocol E and II - eye of healthy volunteer (e-l)) measured with protocol D processed in four different ways: PV – Phase variance angiograms (first column), ACD – Absolute Complex Difference angiograms (second column), SV – Speckle Variance angiograms (third column) and AID – Absolute Intensity Difference (fourth column). The last row presents the human retinal maps obtained for only two B-scans from the group of eight. Brain image size area: 2 mm x 2mm; human eye image size: 1.5 mm x 1.5 mm. Red arrow on (f) shows specular reflection artifact visible also on (g, h, j-l). Comparison between axial phase stabilization and no stabilization in ACD algorithm is visible on (b, f, j) - small insets placed in upper right corners of ACD angiograms show non-stabilized data. Scale bar: 200 μm.

Another parameter of comparison was algorithm complexity. We simulate this parameter through calculating computational time of given implementation. In this comparison intensity

#238344 Received 20 Apr 2015; revised 30 Jun 2015; accepted 30 Jun 2015; published 6 Jul 2015

methods exceeds phase-sensitive ones as seen in Fig. 2(e). Comparing to the fastest AID other methods are 12% (SV), 194% (ACD) and 407% (PV) slower.

In order to verify our quantitative analysis we performed *in vivo* imaging using two different objects: a murine brain and a retina of healthy volunteer. Data were processed in four different ways, described in details in paragraph *2.3*.The results are presented in Fig. 3.

All retinal maps are maximum intensity projections of volumes including retinal layers located inner to IS/OS layer (photoreceptors, RPE and choroid were cropped-out).Only for ACD method the axial phase shift correction algorithm [38] was implemented. It is obvious that all compared algorithms are going to be sensitive to bulk motion occurring during data acquisition. The object motion registered between oversampled B-scans (horizontal axis) manifests as highly intense horizontal stripes, see Fig. 3(f), 3(j). The problem of sample motion is much more severe in the case of *in vivo* eye imaging than in the case of brain imaging since the animal had been anesthetized and stabilized. In immobilized mouse brain images the best contrast of the smallest capillaries in *enface* projection image has been achieved by ACD technique with axial phase shift motion compensation, which is in agreement with results from Fig. 2(c) (red dashed line). SV gives almost similar quality but with slightly higher level of background signal. Result of AID method is comparable to ACD but without any requirement of phase shift compensation (Fig. 3(b), 3(d)) [38]. Slightly less detailed capillary map is given by PV, see Fig. 3(a), however large vessels are still highly contrasted which is in agreement with the results from Fig. 2.

In motion corrupted measurements of the eye the non-stabilized ACD and SV givethe most significant motion artifacts. In particular, anon-compensated ACD provides poor image quality as seen in upper right corners of Fig. 3(f), 3(j).Again here the phase compensated ACD technique provides the highest contrast of capillary net. In order to use advantages of ACD and simplicity of SV method we choose AID analysis, which helps to better suppress motion artifacts than SV for $N > 2$ oversampled data without application of additional stabilization step which is in agreement with results from Fig. 2(d) (green dashed line).PV gives again slightly less visibility of small capillaries but also here the motion artifacts are less pronounced than the other methods, which confirms our analysis presented in Fig. 2(b), 2(d). Comparing images seen in Fig. 3(e)-3(h) we concluded that ACD and AID provide better contrasted capillaries map than PV and SV. The advantage of PV, in turn, is in the best reduction of the specular reflection signal (Fig. 3(e)) visible in the center of foveal avascular zone (FAZ), see Fig. 3(f)-3(h). Moreover the largest vessels are still highly contrasted on this image, see Fig. 3(e). On the other hand the advantage of three other techniques is that the analysis is performed along time axes, so in principle the spatial resolution of ACD, SV and AID methods is preserved in all three dimensions.

Another important practical constrain is the resistance of angiographic OCT algorithms to reduction of available amount of data. To test the robustness of four algorithms we applied them to the extreme case - when only two cross-sectional images are used for contrasting the motion. For this purpose the data collected from the eye were decimated 4 times to obtain 2 times oversampling, see Fig. 3(i)-3(l). Now the differences between angiographic maps are more subtle. The visibility of small capillaries is comparable for all of the methods. It has to be stressed that AID and SV in this case ($N = 2$) give the same result to within a constant. Taking into account the computing efficiency of AID technique we decided to demonstrate applicability of this simple and robust algorithm in clinical cases in diseased eyes (what has not been demonstrated up to date).

3.2. Angio-OCT imaging of the healthy retina

Absolute intensity difference algorithm applied to the healthy retina enables to visualize large retinal vessels along with a dense capillary network, see Fig. 4(c). The dark area within the central macula corresponds to the foveal avascular zone. The demarcating line of the zone is formed by the capillary annulus which extend further towards the angiogram periphery. The

#238344 Received 20 Apr 2015; revised 30 Jun 2015; accepted 30 Jun 2015; published 6 Jul 2015

vascular outline in AID angio-OCT angiography highly corresponds to vascular image obtained in FA. However, the visibility of the capillaries in AID angio-OCT does not change with the increasing distance from the central fovea and it is significantly better in the peripheral macula as compared to FA.

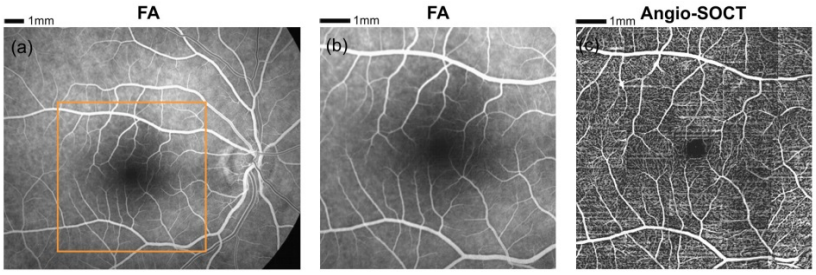

Fig. 4. (a) Fluorescein angiography showing the fundus of a healthy 38-year-old individual. (b) 7.5 x 7.5 mm region of FA corresponding to OCT measurement (c) Angio-OCT fundus view composed of 25-element mosaic (protocol B). The image was created by merging 12,000 B-scans, the total number of A-scans was 2,880,000. Angio-OCT imaging region - 7.5 x 7.5 mm.

3.3. Angio-OCT imaging of diabetic retinopathy and retinal vein occlusion

The AID angio-OCT images of capillary network in patients with Diabetic Retinopathy (DR) and Branch Retinal Vein Occlusion (BRVO) correspond to FA findings are presented in Figs. 5–8. If no significant structural abnormalities are present within the macula, it is easier to identify the capillaries outside the central macula using AID angio-OCT rather than FA. Both methods easily show the enlargement of foveal avascular zone in exactly the same manner, see Fig. 5(c)-5(d), Fig. 6(c)-6(d) and Fig. 7(c)-7(d).However, at the same time the OCT offers an additional advantage of imaging each retinal vascular layer separately, what is presented in panel (f) in Figs. 5–8. Likewise, the sizes and shapes of non-perfusion areas imaged using the two techniques are highly similar, see Fig. 8(c)-8(d).

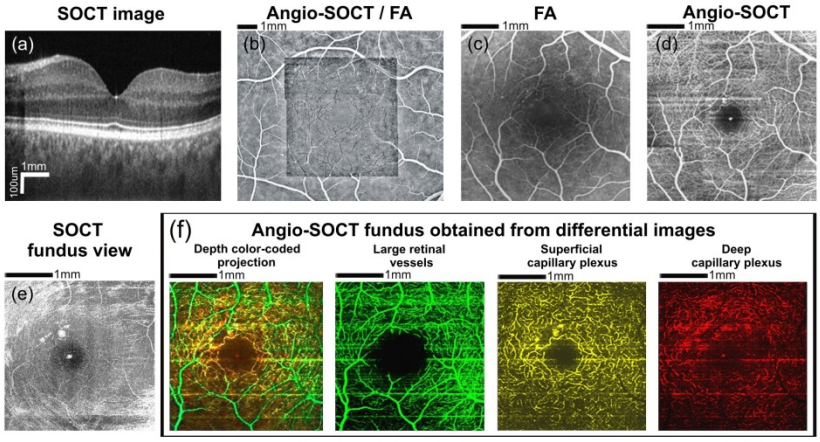

Fig. 5. Data obtained from a 46 year-old patient with diabetic retinopathy. Visual acuity in the right eye was 20/25. (a) OCT cross-sectional image (protocol C). (b) The automatically generated OCT mosaic projected onto the fluorescein angiography image (protocol B). (c) Fluorescein angiography. (d) Angio-OCT mosaic size - 4.5 x 4.5 mm. The tiny white area in the center corresponds to the foveal specular reflex. (e) OCT fundus view (protocol A). (f) Color-coded angio-OCT fundus views showing retinal vasculature at different levels (protocol A). Large retinal vessels were coded green, the superficial capillary plexus was coded yellow and the deep capillary plexus was coded red. It should be noted that the blood vessels of the superficial capillary plexus mark the edge of the foveal avascular zone. Angio-OCT imaging region- 4 x 4 mm.

#238344 Received 20 Apr 2015; revised 30 Jun 2015; accepted 30 Jun 2015; published 6 Jul 2015

In FA imaging the hyperfluorescence of laser scars precludes precise assessment of adjacent capillaries. Thus, it is impossible to precisely determine whether there are non-perfusion areas at these places. Figure 6 shows that secondary lesions within the RPE formed as a result of laser treatment, do not obscure the outline of overpassing capillaries in angio-OCT due to possibility of depth segmentation (Fig. 6(d)). Additionally, Figs. 6 and 7 show that angio-OCT visualizes hard exudates, whose spatial relationship relative to retinal vessels can be seen in AID angio-OCT maps of individual vascular plexus layers, (Figs. 6(f), 7(f)).These static structures (as well as foveal reflex) are not fully suppressed in AID angio-OCT is due to method imperfections discussed in paragraph *3.1*.and analyzed in Figs. 2(b), 2(d). However, in this particular case such imperfection can be used as additional clinically relevant marker.

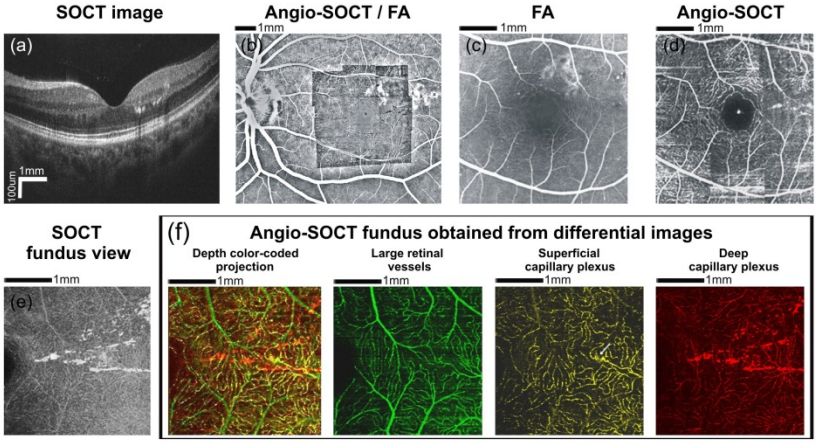

Fig. 6. Data obtained from a 37 year-old patient with diabetic retinopathy. Visual acuity in the left eye was 20/25. (a) OCT cross-sectional image (protocol C). Hard exudates are visible in the temporal macula. (b) The automatically generated angio-OCT mosaic projected onto the fluorescein angiography image (protocol B). (c) Fluorescein angiography showing few microaneurysms. The capillary network pattern above and temporally from the fovea is obscured by the hyperfluorescence of laser scars. Hard exudates are not visible in FA image. (d) AID angio-OCT mosaic of the fundus area shown in Fig. 6(c). Laser scars do not obscure retinal vasculature as angio-OCT scans do not include RPE-generated signal. Few microaneurysms and several hard exudates are visible within temporal macula. The white punctate spot in the center corresponds to foveal reflex. Angio-OCT imaging region - 4.5 x 4.5 mm. (e) OCT fundus view of temporal macula with the hard exudates (protocol A).(f) Color-coded angio-OCT fundus views showing retinal vasculature at different levels (layers) within the temporal macula (protocol A). Large retinal vessels were coded green, the superficial capillary plexus was coded yellow and the deep capillary plexus was coded red. It is clearly visible that most hard exudates are located within the deep capillary plexus. Superficial capillary plexus is the source of hard exudates at a single site only (arrow). Angio-OCT imaging region - 3.1 x 3.1 mm.

Microaneurysms visualization appears to be a significant challenge in angio-OCT, at least using the presented technique. OCT angiograms visualize the "motion" during oversampled period. OCT signal modulation during time acquisition within the blood vessels is mostly due to blood cells flow. If plasma-transported RBCs fail to enter the microaneurysms or the dynamics of this flow is very slow, therefore it is rather not possible to visualize microaneurysms using current angio-OCT. Difficulties in the visualization of microaneurysms is also reported using pvOCT [33]. On the other hand, FA does not reveal hard exudates, which are clearly visible on the OCT structural images (Figs. 6 and 7).

#238344 Received 20 Apr 2015; revised 30 Jun 2015; accepted 30 Jun 2015; published 6 Jul 2015

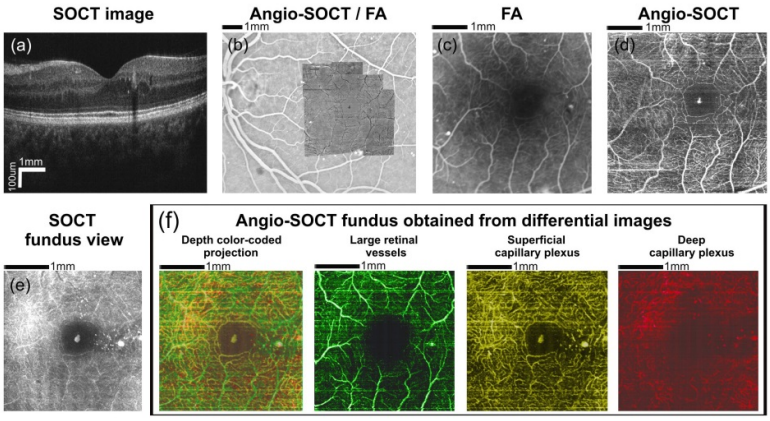

Fig. 7. Data obtained from a 53 year-old patient with diabetic retinopathy. Visual acuity in the left eye was 20/32. (a) OCT cross-sectional image (protocol C). Hard exudates are visible in the temporal macula. Adjacent to the exudates, a single intraretinal fluid space is shown. (b) The automatically generated angio-OCT mosaic projected onto the fluorescein angiography image (protocol B). (c) A fluorescein angiography showing a few micro aneurysms. Hard exudates are not visible. (d) Angio-OCT mosaic of the fundus area shown in Fig. 7(c). Single hard exudates are visible within the temporal macula. The white area in the center corresponds to foveal reflex. Angio-OCT imaging region - 4.5 x 4.5 mm. (e) OCT fundus view revealing the hard exudates (protocol A).(f) Color-coded angio-OCT fundus views showing macular vasculature at different levels (layers) (protocol A). Large retinal vessels were coded green, the superficial capillary plexus was coded yellow and the deep capillary plexus was coded red. Tiny hard exudates seen within temporal and superior macula are located in the deep capilary plexus layer. Furthermore, there is another hard exudates deposit within temporal macula, located in the superficial capillary plexus layer. It should be noted that the blood vessels of the superficial capillary plexus mark the edge of the foveal avascular zone. Angio-OCT imaging region - 3.1 x 3.1 mm.

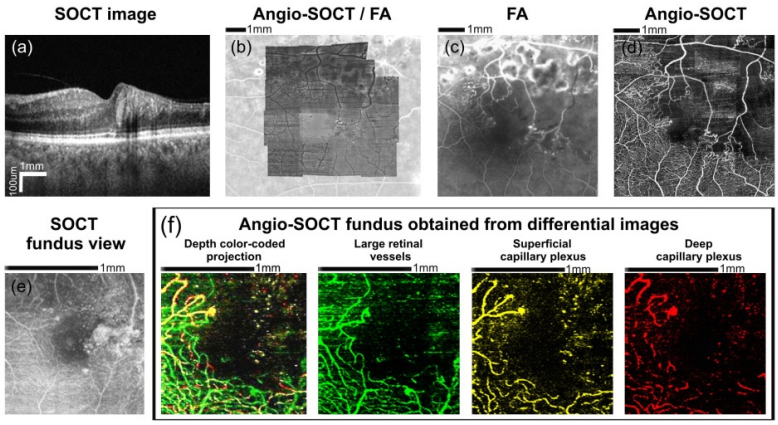

Fig. 8. Data obtained from a 55 year-old patient with branch retinal vein occlusion. Visual acuity in the left eye was 20/100. (a) OCT cross-sectional image shows the decreased retinal thickness within the temporal macula (protocol C). (b) The automatically generated angio-OCT mosaic projected onto the fluorescein angiography image (protocol B). (c) Fluorescein angiography image (d) Angio-OCT mosaic of the fundus area shown in Fig. 8(c). An extensive non-perfusion area is clearly visible. Angio-OCT imaging region - 6 x 6 mm. (e) OCT fundus view showing changes of retinal reflectivity (protocol A). (f) Color-coded angio-OCT fundus views showing retinal vasculature at different levels (layers) within the temporal macula (protocol B). Large retinal vessels were coded green, the superficial capillary plexus was coded yellow and the deep capillary plexus was coded red. It is possible to follow the three-dimensional pattern of the retinal capillary network. Angio-OCT imaging region - 1.5 x 1.5 mm.

#238344 Received 20 Apr 2015; revised 30 Jun 2015; accepted 30 Jun 2015; published 6 Jul 2015

Figure 8 shows data obtained from a patient with BRVO. Fluorescein angiography shows an extensive non-perfusion area involving temporal and superior macula. Numerous laser treatment scars are visible within superior macula, which impede capillary outline interpretation. OCT cross-sectional images show significant change in the retinal thickness within the temporal macula. In this case angio-OCT mosaic of the fundus reveals an extensive non-perfusion area corresponding well to FA image. The vessels not filling until the late stage of FA are also visible. Laser scars do not preclude angio-OCT interpretation, as it does not contain the RPE-generated signal.

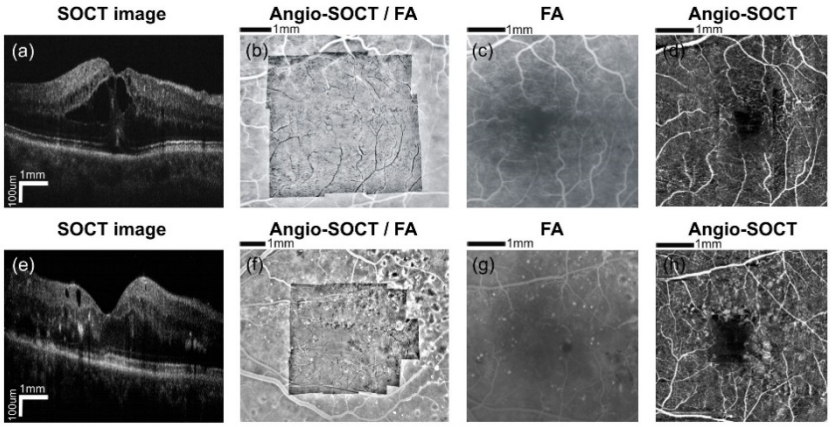

Fig. 9. Diabetic macular edema. The images in the upper row show the 69 year-old patient. Visual acuity in the left eye was 20/63. The images in the bottom row show the 40 year-old patient. Visual acuity in the left eye was 20/80. (a) OCT cross-sectional image showing the intraretinal fluid spaces within the macula (protocol C). (b) The automatically generated angio-OCT mosaic projected onto the fluorescein angiography image (protocol B). (c) The fluorescein angiography presents the enlargement of the foveal avascular zone. Angio-OCT imaging region - 4.5 x 4.5 mm. (d) The angio-OCT mosaic shows the fundus area as seen in Fig. 9(c). The foveal avascular zone is visibly enlarged. (e) OCT cross-sectional image showing a few intraretinal fluid spaces, located in the inner retinal layers within the macula (protocol C). (f) The automatically generated angio-OCT mosaic projected onto the fluorescein angiography image (protocol B). (g) The fluorescein angiography presents the enlargement of the foveal avascular zone and the non-perfusion areas. (h) The angio-OCT mosaic shows the fundus area as seen in Fig. 8(g). The foveal avascular zone is visibly enlarged. Adjacent to the avascular zone, the non-perfusion areas are shown. Angio-OCT imaging region - 4.5 x 4.5 mm.

OCT is also capable of revealing the areas of macular ischemia in patients with significant macular edema and retinal structural abnormalities, see Fig. 9. AID angio-OCT performs acceptably well even in such cases, revealing ischemic areas, which could have been previously shown only in an invasive FA. Nevertheless, it should be emphasized that AID angio-OCT may be particularly difficult to perform and its findings may not be easy to interpret in eyes with extensive macular edema and significant retinal structural abnormalities.

Unlike FA, the OCT angiography technique allows appreciation of spatial relationships of fundus vessels and makes it possible to separately visualize the large retinal vessels as well as the superficial capillary plexus and the deep capillary plexus. However during maximum intensity projection from structural data capillaries are visible in Figs. 5(e), 6(e), 7(e), 8(e) in similar way to previous work [25], further motion contrasted AID analysis helps to improve image contrast and suppress hyper reflective motionless structures, see Figs. 5(d), 5(f), 6(d), 6(f), 7(d), 7(f), 8(d), 8(f). This, in turn, provides an insight into the three-dimensional structure of the capillary network, which may give a rise to the new *in vivo* studies of vascular pathology in retinal diseases.

#238344 Received 20 Apr 2015; revised 30 Jun 2015; accepted 30 Jun 2015; published 6 Jul 2015

4. Discussion and conclusions

In this contribution we demonstrate comparison between four OCT angiography techniques: phase variance (PV), absolute complex difference (ACD), speckle variance (SV)and absolute intensity difference (AID). Contrast-to-noise analysis confirmed high performance of phase-sensitive (PV, ACD) methods in generation flow motion contrast, however these methods require more advanced analysis than intensity-based ones (SV, AID).Resistance to motion artifacts of non-stabilized data is in following order: PV, AID, SV and ACD. In case of only two times oversampled data AID and SV provide the same properties. However, in case of highly data oversampling (N>2) SVis less resistant to motion artifacts comparing to AID. In this case AID also allows to obtain images faster and brings high quality of OCT angio-maps, that is especially important in the early diagnosis of retinal vascular diseases.

We also present an ophthalmic application of the absolute intensity difference technique (AID) on healthy as well as diseased eyes, where only two B-scans are collected from the same spatial location on the retina. The results that we have obtained were compared with fluorescein angiography showing high correspondence. Our data also suggests that, in some cases, the intensity-based OCT angiogram shows more capillaries in the pericentral macula than FA. Furthermore, with OCT different retinal layers can be resolved and non-perfusion areas can be easily identified.

Although the AID algorithm is computationally efficient, the RPE segmentation and segmented flow image cropping has to be additionally performed to improve capillaries visualization. This may be considered as a limiting factor. However, we assumed that the most of clinically available OCT systems include algorithms for segmentation of retinal layers with high precision. Also receiving wide-field mosaic angiograms is challenging because it requires additional acquisition and processing time. Our SOCT device has not yet been equipped with the eye tracking system. That is why we focused on small but fast multiple measurements that can be integrated on wide-field mosaic. Implementation of the eye tracking set-up may help to obtain wide-field angiographic data comparable to the wide-field FA.

Acknowledgments

Supported by: the TEAM project (MW, DR) financed by European Union within the frames of Innovative Economy coordinated by for Foundation Polish Science, National Center for Research and Development Grant No. PBS1/A9/20/2013 (DR, MS, KK), grant of the Institute of Physics NCU, Step into Future project (BLS, DB, DR), NCU Chancellor's research grant (BLS). Funding organizations had no role in the design or conduct of this research. We thank Iwona Gorczynska for making the setups available for measurements, Grzegorz Wilczynski for providing biological samples. Daniel Szlag and Marcin Sylwestrzak for providing data acquisition software, Daniel Szlag and Arno Bouwens for data analysis consultation.

#238344 Received 20 Apr 2015; revised 30 Jun 2015; accepted 30 Jun 2015; published 6 Jul 2015